

An Investigation of Plasma Chemistry for dc Plasma Enhanced Chemical Vapor Deposition of Carbon Nanotubes and Nanofibers

*David B. Hash,¹ Martin S. Bell,² Kenneth B. K. Teo,² Brett A. Cruden,¹ William I. Milne,²
and M. Meyyappan^{†1}*

¹Center for Nanotechnology, NASA Ames Research Center, Moffett Field, California
94035, USA

²Department of Engineering, University of Cambridge, Cambridge CB2 1PZ, United
Kingdom

The role of plasma in plasma enhanced chemical vapor deposition of carbon nanotubes and nanofibers is investigated with both experimental and computational diagnostic techniques. A residual gas analysis (RGA) of a 12 mbar direct current (dc) discharge with a C₂H₂/NH₃ gas mixture is conducted near the Ni catalyst surface employed for carbon nanofiber growth. The results are corroborated with a 1-D dc discharge model that solves for species densities, ion momentum, and ion, electron, and neutral gas thermal energies.

[†] Corresponding author. E-mail: M.Meyyappan@nasa.gov.

The effect of varying the plasma power from 0 to 200 W on the gas composition is studied. The dissociation efficiency of the plasma is demonstrated where over 50 percent of the feedstock is converted to a mixture of hydrogen, nitrogen, and hydrogen cyanide at 200 W. Finally, the important role that endothermic ion-molecule reactions play in this conversion is established for the first time. Of these reactions, dissociative proton abstraction and collision-induced dissociation are of the greatest significance.

1. Introduction

Catalytic decomposition of carbon-bearing gases on metallic nanocluster catalysts in chemical vapor deposition (CVD) systems for growth of carbon nanotubes and nanofibers combines the advantages of low-temperature (relative to arc discharge and laser ablation), low-cost, and commercial-scale production with the ability to pattern growth through lithographic positioning of transition metal catalysts on substrates. Many potential applications of nanotubes such as atomic force microscope tips [1], superhydrophobic surfaces [2], field emission cathodes [3,4], vertical interconnects [5,6], electron beam lithography [7,8,9,10], synthetic membranes [11,12], intracellular gene delivery devices [13,14], and nanoelectrode electrochemical probes and biosensors [15,16,17,18,19] require not only patterned growth but also vertical alignment. Alignment in thermal CVD processes can be obtained through van der Waals interaction-sponsored alignment where carbon nanotubes are grown closely together like towers or through template-assisted growth. However, the application of large electric fields provides superior alignment [20,21,22,23,24] by inducing dipole moments preferentially along the axes of carbon nanotubes that act to align the tube in the direction of the field and combat any randomizing effect of thermal vibrations. Electric field enabled

alignment is exploited in plasma enhanced CVD (PECVD) with various configurations including dc [25,26,27,28,29,30,31], radiofrequency [32,33,34,35], microwave [36,37,38], inductive [39,40,41,42,43,44], and electron cyclotron resonance [45,46,47]. Lin *et al.* [48] demonstrated that the alignment mechanism is the same for all systems. Regardless of whether a system employs a microwave plasma with a self-bias of 10 V and sheath width on the order of 100 μm or a dc discharge with 600 V applied bias and 2 mm sheath width, the sheath electric fields are on the same order and are requisite for aligned growth. The plasma itself, in fact, is not required for aligned growth as references [21] and [22] employed fields through small applied voltages (3-20 V) across very small electrode spacings (10-100 μm) and thus avoided striking a discharge. This demonstrates that the only requirement for aligned growth is an electric field and that it is the sheath electric field of the plasma and not the plasma itself that affects alignment. However, large-scale electric field aligned nanotube production has yet to be accomplished without a plasma; and thus, as it is at present unavoidable for large-scale superiorly aligned growth, it is important to understand the comprehensive role of the plasma. Specifically, the present work examines the effect of the plasma chemistry on gas composition in dc PECVD and thus the subsequent precursors to nanotube growth. The investigation relies on both experimental and computational methods to perform plasma diagnostics. Within the computational approach, the importance of modeling sheath endothermic ion-molecule reactions is examined. The experimental approach involves a residual gas analysis (RGA) study of the plasma and adds to the growing, but still limited work in this area [49,50,51,52,53].

2. CNT Growth

The reactor employed for this study is a simple dc configuration of equal area (10 cm^2) cathode and anode with a 5 cm separation. The feedstock of 54:200 sccm of $\text{C}_2\text{H}_2/\text{NH}_3$ is injected through a showerhead, which also acts as the anode. The graphite cathode has an embedded rigid tungsten wire heater coupled with an electrically isolated thermocouple to allow independent temperature control of the substrate if necessary.

Si<100> substrates were coated with conductive indium tin oxide (15 nm thick) and Ni (7 nm) thin films by magnetron sputtering. The substrate was placed on the cathode and a dc glow discharge was initiated at low power and pressure (20 W, 2.5 mbar) in pure NH_3 . The power and pressure were then simultaneously increased to 120 W and 12 mbar respectively, and a cathode temperature of $550\text{ }^\circ\text{C}$ was typically obtained after just one minute. This catalyst pretreatment procedure transformed the Ni thin film into nanoclusters of the range between 50 to 100 nm. After the one minute NH_3 plasma-annealing step, C_2H_2 was introduced into the gas mixture and growth was performed at the desired plasma power for 15 minutes. All cases reported were performed at a pressure of 12 mbar, and the desired plasma power in the range of 20 to 200 W was achieved by varying the applied dc bias from 470 to 650 V. The substrate is heated solely by the plasma, and its temperature varies between 350 and $715\text{ }^\circ\text{C}$ over the power range investigated though the low range is not suitable for growth.

3. Computational Model

The role of the plasma is investigated with a 1-D radially averaged computational model [54]. Equations for the conservation of species mass, ion momentum, and ion, electron, and neutral gas thermal energy are solved axially between the two electrodes.

The model includes 21 neutral species (H_2 , H , CH_4 , CH_3 , CH_2 , CH , C_2H_4 , C_2H_3 , C_2H_2 , C_2H , N_2 , N , NH_3 , NH_2 , NH , NNH , HCN , CN , HC_3N , H_2CN , H_2CNH), seven charged species (NH_3^+ , NH_2^+ , C_2H_2^+ , C_2H^+ , H_2^+ , H^+ , e), and 200 reactions. As a boundary condition for the gas energy equation, a cathode energy balance is incorporated to model ion bombardment, thermal radiation, and solid and gas conduction to predict the cathode temperature.

The computational model includes endothermic ion-molecule reactions that have not been investigated in simulations heretofore. Inclusion of these reactions requires the addition of the ion momentum and energy equations to compute both the directed and thermal energies of the ions. Endothermic ion-molecule reactions only occur in the sheath where ions have energies larger than the reaction barrier. Studies of low-pressure discharges for semiconductor applications, in which sheaths are collisionless, have often neglected endothermic ion-molecule reactions while including exothermic ones. Peko *et al.* [55] advocated for the inclusion of ion-molecule reactions in simulations, as they are “essential because of the important role that secondary products from ion-molecule reactions play in the etching and deposition processes.” This is especially true in nanotube processing where sheaths are collisional because of higher operating pressures (~ 10 mbar) and ion energies are significant because of the large applied biases (~ 500 V) required for alignment such that both exothermic and endothermic ion-molecule reactions are important. Table 1 displays the rates employed for exothermic ion-molecule reactions, and the endothermic rates for charge transfer, dissociative charge transfer, dissociative proton abstraction, and collision-induced dissociation are given in Table 2. Rates for the exothermic reactions are easily found in the modeling literature of planetary

atmospheres; however, rates of endothermic ion-molecule reactions for most nanotube processing gases are not available. As a result, the rates of these reactions for methane from the work of Peko *et al.* [56] were used as estimates for acetylene and ammonia, where the experimentally measured cross-sections reported for these reactions were integrated over a Maxwellian distribution and then fit to the Arrhenius form.

4. Experimental Diagnostics

Mass spectrometry was performed one centimeter from the cathode using a Hiden EQP High Energy plasma analyzer, differentially pumped to 1×10^{-6} mbar. For neutral species measurements, the acquired mass spectra must be deconvolved, as the resulting intensities, i , from the RGA are products of the original species cracking patterns. For a system of n species and m spectra, the following matrix [57] must be solved for $[I]$

$$\begin{bmatrix} i_1 \\ i_2 \\ \vdots \\ i_m \end{bmatrix} = \begin{bmatrix} a_{11} & \bullet & \bullet & \bullet & a_{1n} \\ a_{21} & \bullet & \bullet & \bullet & a_{2n} \\ \bullet & \bullet & \bullet & \bullet & \bullet \\ a_{m1} & \bullet & \bullet & \bullet & a_{mn} \end{bmatrix} \begin{bmatrix} I_1 \\ I_2 \\ \vdots \\ I_n \end{bmatrix} \quad (1)$$

where a represents the cracking patterns for each of the n species. The 70 eV cracking patterns are taken from the NIST Chemistry WebBook [58]. To avoid overfitting the data, n was limited to 17 species, which best fit the data and were consistent with the modeling results.

5. Results and Discussion

Figures 1 and 2 display the percent decomposition of the feedstock gases, ammonia, and acetylene, as a function of plasma power. It is defined as the percent change in mole fraction relative to the plasma off condition

$$\frac{X_s^* - X_s}{X_s^*} = \frac{P_s^*/P^* - P_s/P}{P_s^*/P^*} \quad (2)$$

where X_s is the mole fraction of species s , $*$ denotes the plasma off condition, and P_s is the partial pressure of species s . Given that the total pressure is maintained constant for all the cases considered and the intensities from the RGA are proportional to the partial pressures, Eq. (2) can be rewritten as

$$\frac{X_s^* - X_s}{X_s^*} = \frac{I_s^* - I_s}{I_s^*}. \quad (3)$$

In the figures, three separate sets of data are displayed: the RGA measurements, the simulation with the full reaction set, and the simulation with a reduced reaction set excluding the endothermic ion-molecule reactions. For ammonia, the comparison between the experiment and the full simulation is good between 0 and 100 W but suffers at high powers. For acetylene, even the full simulation is not able to reproduce the experimental result where over 80 percent of the feedstock acetylene is decomposed at the highest plasma power. Possible reasons for the discrepancy may include approximations in the RGA analysis, rate estimates used for ion-molecule reactions, or loss of carbon to surface reactions. Of these, the rate estimates used are the most probable source of error. Because cross section measurements for endothermic ion-molecule reactions in acetylene and ammonia cannot be found in the literature, the exact same rates for these reactions were employed for both gases. Thus, it is likely that the methane rates employed more accurately represent ammonia ion-molecule reaction rates than that of acetylene, explaining the more accurate comparison to experiment for ammonia than for acetylene. Despite these possible shortcomings, these plots provide an important insight into some of the relevant plasma chemistry, namely the importance of incorporating endothermic ion-molecule reactions into the model. The percent difference between the simulations with and without these reactions is quite significant, ranging from 50 to 200

percent with the full simulations providing a better comparison to the experiment for both ammonia and acetylene. Figures 3 and 4 display the ion loss rate for each of the endothermic ion-molecule reactions employed for ammonia and acetylene across the electrode spacing. The rate axis is plotted logarithmically, dramatically demonstrating that these reactions occur solely in the 1.5 mm sheath adjacent to the cathode. For both ammonia and acetylene, the dominant endothermic ion-molecule reaction is dissociative proton abstraction followed by collision-induced dissociation. At least these two reaction mechanisms should be included in simulations of dc discharges for nanotube processing to obtain reliable results.

Figure 5 shows the mole fraction trends with plasma power for the three main plasma products: H_2 , N_2 , and HCN. To compare the experiment with the simulations, the experimental data are calibrated to the simulation at the 100 W midpoint. The simulation results displayed here are from the full reaction set employing all ion-molecule reactions. The trends are reproduced well where hydrogen and hydrogen cyanide increase with increasing power and nitrogen remains relatively flat. The exception is HCN at lower powers where the simulation shows a much larger increase in HCN than the experiment. HCN is formed primarily from the reaction $CH + HCN \rightleftharpoons N + C_2H_2$ whose equilibrium constant derived backward reaction rate in the simulation was calculated from a published [59] estimated forward reaction rate of $1.66 \times 10^{-10} \text{ cm}^3/\text{sec}$. The region of discrepancy between 0 and 50 W has a significant gas temperature rise, and it may be that in actuality, the reaction has a temperature dependence that would mitigate the differences between the experiment and simulation.

Figure 6 illustrates the significant role plasma plays in nanotube processing. The simulated mole fractions of the seven most dominant stable species are shown with the three most significant radicals over the electrode spacing at the highest plasma power investigated (200 W). The ammonia and acetylene feedstock gases dissociate near the cathode in the high-energy sheath region resulting in the highest concentration of radicals. At this power, the plasma can convert enough of the acetylene into hydrogen cyanide to make it the most dominant carbon-bearing species at the cathode. Figure 7 is a similar plot in which the species number densities at the cathode where the substrate is positioned are plotted versus plasma power. Here, it is clear that the growth sample will see more HCN than C_2H_2 . The dramatic impact this has on growth has been previously demonstrated [60], whereby, at the same substrate temperature, higher power conditions result in much shorter nanofibers relative to lower power growth conditions. The lower growth rate was attributed to acetylene decomposing more readily on Ni catalyst than HCN given that the C-N triple bond strength [61] is 748 kJ/mol and the H-CCH bond strength is only 556 kJ/mol.

6. Conclusions

The role of plasma in dc plasma enhanced chemical vapor deposition of carbon nanofibers has been investigated both experimentally and computationally. Both demonstrate the significant role plasma plays in determining the gas-phase species impinging on the catalysts. The diagnostics show that a 12 mbar, 200 W dc discharge with a 5 cm electrode gap and 10 cm² area efficiently dissociates the ammonia and acetylene feedstock gases by as much as 50-60 percent and 60-80 percent, respectively. The resulting new carbon-bearing species (hydrogen cyanide, methanimine, and

methane) will catalyze at different rates than the original feedstock, thus impacting final growth rates. Depending on the feedstock gas mixture and the catalyst employed, this feedstock conversion may or may not be advantageous. In our case where Ni catalyst was used, the generation of hydrogen cyanide at the expense of acetylene at higher powers actually impeded the nanotube/fiber growth rate, in contrast to conventional thinking which assumes higher plasma powers would lead to more efficient/higher growth rates. The result is that the term plasma enhanced CVD becomes a misnomer where the plasma chemistry actually results in decreased growth rates. In order to produce optimal growth conditions with the C_2H_2/NH_3 gas mixture, the plasma power is maintained low enough to reduce the degree of gas conversion while still high enough to guarantee superior alignment from the plasma sheath fields.

For the first time, the important role of endothermic ion-molecule reactions has been demonstrated in plasma-assisted nanotube processing. In many applications, these reactions can be and have been ignored as they occur only in the sheaths and require significant pressures and ion energies. The high pressures (~ 10 mbar) and high applied dc biases (~ 500 V) in nanotube processing however present the perfect condition for these reactions, and it is demonstrated here that neglecting them may lead to errors in prediction of gas phase composition on the order of a factor of two.

Acknowledgments

M.S.B. acknowledges support from the Engineering and Physical Sciences Research Council (EPSRC), UK. K.B.K.T. acknowledges the support of the Royal Academy of Engineering and Christ's College, Cambridge. B.A.C is supported by the University Affiliated Research Center (UARC) at NASA Ames operated by the University of

California at Santa Cruz under contract NAS2-031434. Discussions with Alan M. Cassell and Charles W. Bauschlicher, Jr. are acknowledged.

Table 1. Exothermic Ion-Molecule Reactions

Reaction	Rate (cm ³ /sec)	Reference
Charge Transfer		
$\text{H}^+ + \text{NH}_3 \rightarrow \text{NH}_3^+ + \text{H}$	5.2×10^{-9}	62
$\text{H}_2^+ + \text{H} \rightarrow \text{H}^+ + \text{H}_2$	6.4×10^{-10}	62
$\text{H}_2^+ + \text{C}_2\text{H}_2 \rightarrow \text{C}_2\text{H}_2^+ + \text{H}_2$	4.82×10^{-9}	62
$\text{H}_2^+ + \text{NH}_3 \rightarrow \text{NH}_3^+ + \text{H}_2$	5.7×10^{-9}	62
$\text{C}_2\text{H}^+ + \text{NH}_3 \rightarrow \text{NH}_3^+ + \text{C}_2\text{H}$	1.6×10^{-9}	63
$\text{NH}_2^+ + \text{NH}_3 \rightarrow \text{NH}_3^+ + \text{NH}_2$	1.8×10^{-9}	64
Proton abstraction		
$\text{C}_2\text{H}^+ + \text{H}_2 \rightarrow \text{C}_2\text{H}_2^+ + \text{H}$	1.24×10^{-9}	62
$\text{C}_2\text{H}^+ + \text{CH}_4 \rightarrow \text{C}_2\text{H}_2^+ + \text{CH}_3$	3.74×10^{-10}	62
$\text{C}_2\text{H}^+ + \text{C}_2\text{H}_4 \rightarrow \text{C}_2\text{H}_2^+ + \text{C}_2\text{H}_3$	1.71×10^{-9}	65
$\text{C}_2\text{H}^+ + \text{HCN} \rightarrow \text{C}_2\text{H}_2^+ + \text{CN}$	5.4×10^{-10}	62
$\text{NH}_2^+ + \text{H}_2 \rightarrow \text{NH}_3^+ + \text{H}$	1.95×10^{-10}	62
$\text{NH}_2^+ + \text{CH}_4 \rightarrow \text{NH}_3^+ + \text{CH}_3$	9.2×10^{-10}	62
Dissociative Charge Transfer		
$\text{H}_2^+ + \text{C}_2\text{H}_4 \rightarrow \text{C}_2\text{H}_2^+ + \text{H}_2 + \text{H}_2$	8.82×10^{-10}	62
Other		
$\text{H}^+ + \text{C}_2\text{H}_2 \rightarrow \text{C}_2\text{H}^+ + \text{H}_2$	4.3×10^{-9}	66
$\text{H}_2^+ + \text{NH} \rightarrow \text{NH}_2^+ + \text{H}$	7.6×10^{-10}	66

Table 2. Endothermic Ion-Molecule Reactions

Reaction	Rate (cm ³ /sec)	Reference
Charge Transfer		
$\text{H}^+ + \text{H}_2 \rightarrow \text{H}_2^+ + \text{H}$	$1.57 \times 10^{-9} \text{T}^{-0.13} \exp(-2.9/\text{T})$	67
$\text{C}_2\text{H}_2^+ + \text{H}_2 \rightarrow \text{H}_2^+ + \text{C}_2\text{H}_2$	$4.0 \times 10^{-9} \text{T}^{-0.25} \exp(-14.6/\text{T})$	56 ^a
$\text{NH}_3^+ + \text{H}_2 \rightarrow \text{H}_2^+ + \text{NH}_3$	$4.0 \times 10^{-9} \text{T}^{-0.25} \exp(-14.6/\text{T})$	56 ^a
Collision-induced Dissociation		
$\text{C}_2\text{H}_2^+ + \text{C}_2\text{H}_2 \rightarrow \text{H}^+ + \text{C}_2\text{H} + \text{C}_2\text{H}_2$	$1.81 \times 10^{-9} \text{T}^{-0.17} \exp(-4.6/\text{T})$	56 ^a
$\text{NH}_3^+ + \text{NH}_3 \rightarrow \text{H}^+ + \text{NH}_2 + \text{NH}_3$	$1.81 \times 10^{-9} \text{T}^{-0.17} \exp(-4.6/\text{T})$	56 ^a
$\text{C}_2\text{H}_2^+ + \text{H}_2 \rightarrow \text{H}^+ + \text{C}_2\text{H} + \text{H}_2$	$6.8 \times 10^{-9} \text{T}^{-0.2} \exp(-9.9/\text{T})$	56 ^a
$\text{NH}_3^+ + \text{H}_2 \rightarrow \text{H}^+ + \text{NH}_2 + \text{H}_2$	$6.8 \times 10^{-9} \text{T}^{-0.2} \exp(-9.9/\text{T})$	56 ^a
Dissociative Proton Abstraction		
$\text{C}_2\text{H}_2^+ + \text{C}_2\text{H}_2 \rightarrow \text{C}_2\text{H}^+ + \text{H}_2 + \text{C}_2\text{H}$	$7.5 \times 10^{-8} \text{T}^{-0.44} \exp(-3.8/\text{T})$	56 ^a
$\text{NH}_3^+ + \text{NH}_3 \rightarrow \text{NH}_2^+ + \text{H}_2 + \text{NH}_2$	$7.5 \times 10^{-8} \text{T}^{-0.44} \exp(-3.8/\text{T})$	56 ^a
Dissociative Charge Transfer		
$\text{H}_2^+ + \text{H}_2 \rightarrow \text{H}^+ + \text{H} + \text{H}_2$	$1.97 \times 10^{-9} \text{T}^{-0.19} \exp(-5.3/\text{T})$	67
$\text{C}_2\text{H}_2^+ + \text{C}_2\text{H}_2 \rightarrow \text{C}_2\text{H}^+ + \text{H} + \text{C}_2\text{H}_2$	$3.7 \times 10^{-9} \text{T}^{-0.3} \exp(-21.1/\text{T})$	56 ^a
$\text{NH}_3^+ + \text{NH}_3 \rightarrow \text{NH}_2^+ + \text{H} + \text{NH}_3$	$3.7 \times 10^{-9} \text{T}^{-0.3} \exp(-21.1/\text{T})$	56 ^a
$\text{C}_2\text{H}_2^+ + \text{H}_2 \rightarrow \text{H}^+ + \text{H} + \text{C}_2\text{H}_2$	$7.8 \times 10^{-9} \text{T}^{-0.39} \exp(-14.8/\text{T})$	56 ^a
$\text{NH}_3^+ + \text{H}_2 \rightarrow \text{H}^+ + \text{H} + \text{NH}_3$	$7.8 \times 10^{-9} \text{T}^{-0.39} \exp(-14.8/\text{T})$	56 ^a

^a estimate from CH₄.

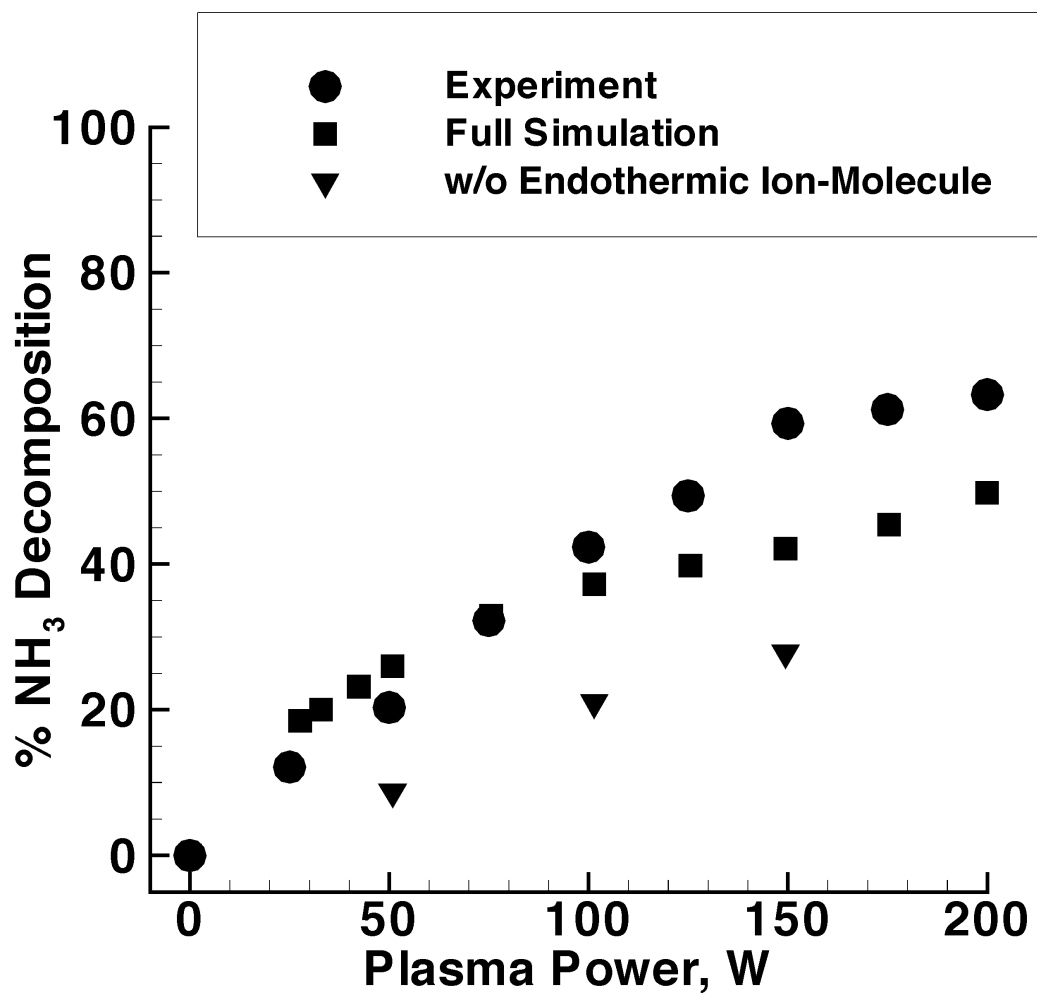


Figure 1. Percent ammonia decomposition at one centimeter from the cathode. The circles are experimental measurements, the squares are the full simulation results including all ion-molecule reactions, and the triangles are the simulation results excluding endothermic ion-molecule reactions.

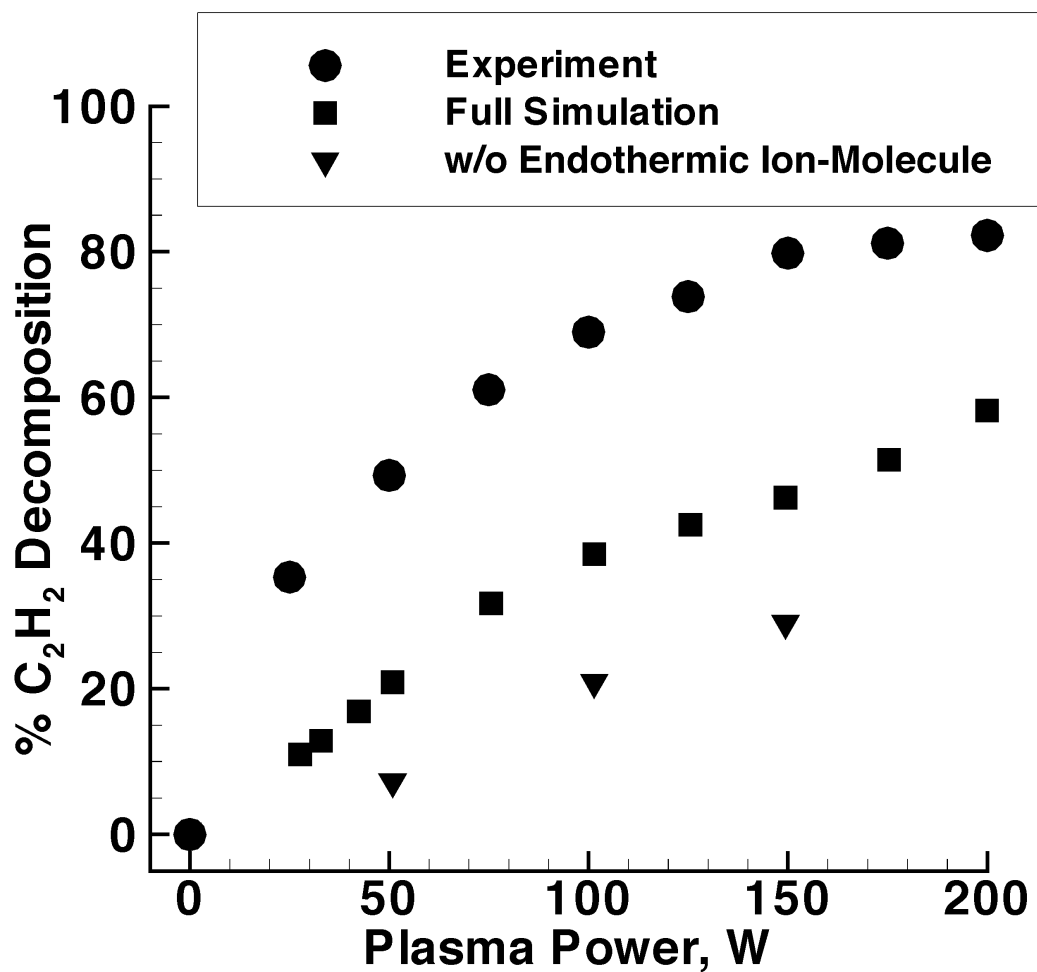


Figure 2. Percent acetylene decomposition at one centimeter from the cathode. The circles are experimental measurements, the squares are the full simulation results including all ion-molecule reactions, and the triangles are the simulation results excluding endothermic ion-molecule reactions.

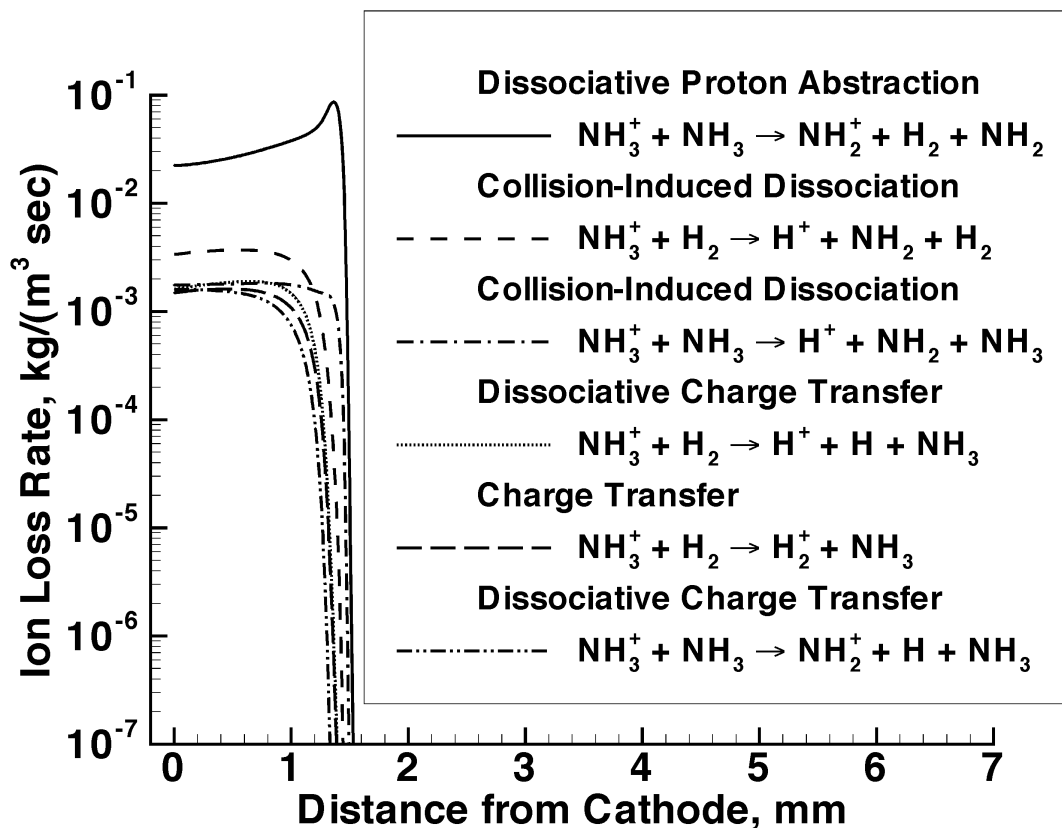


Figure 3. Ammonia ion loss rate from endothermic ion-molecule reactions in the cathode sheath. Dissociative proton abstraction and collision-induced dissociation are the dominant reactions.

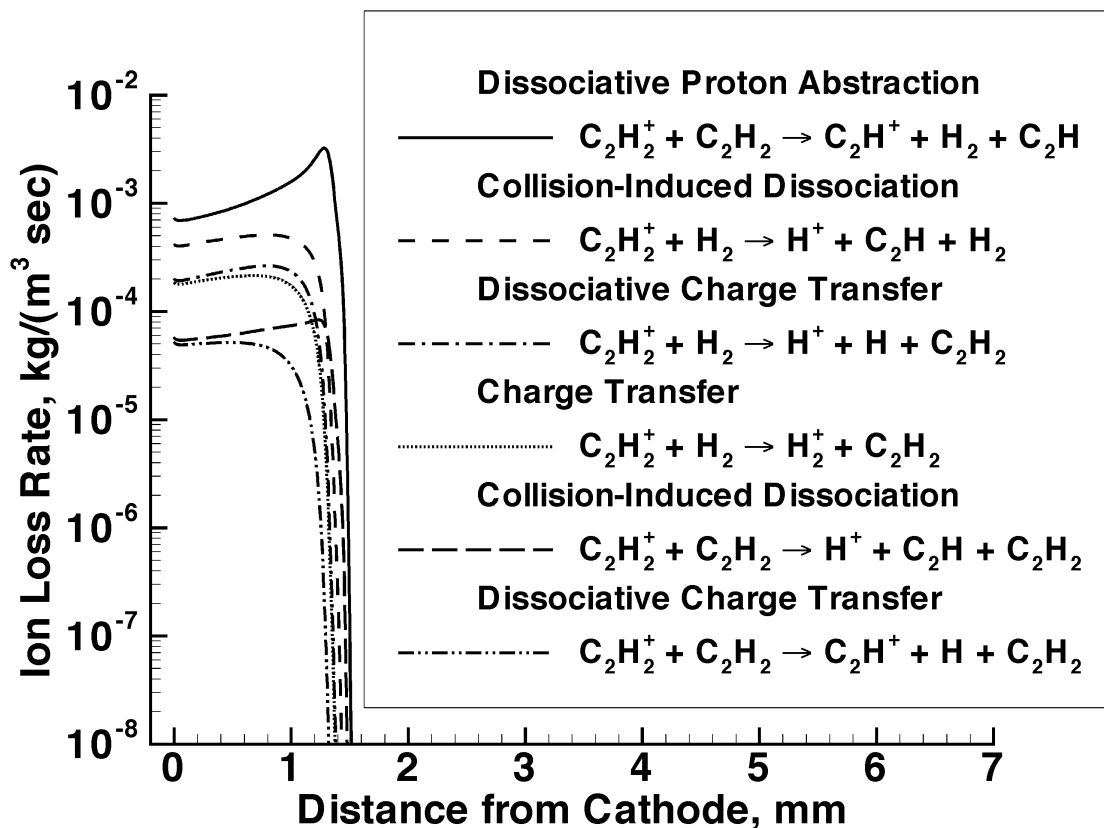


Figure 4. Acetylene ion loss rate from endothermic ion-molecule reactions in the cathode sheath. Dissociative proton abstraction and collision-induced dissociation are the dominant reactions.

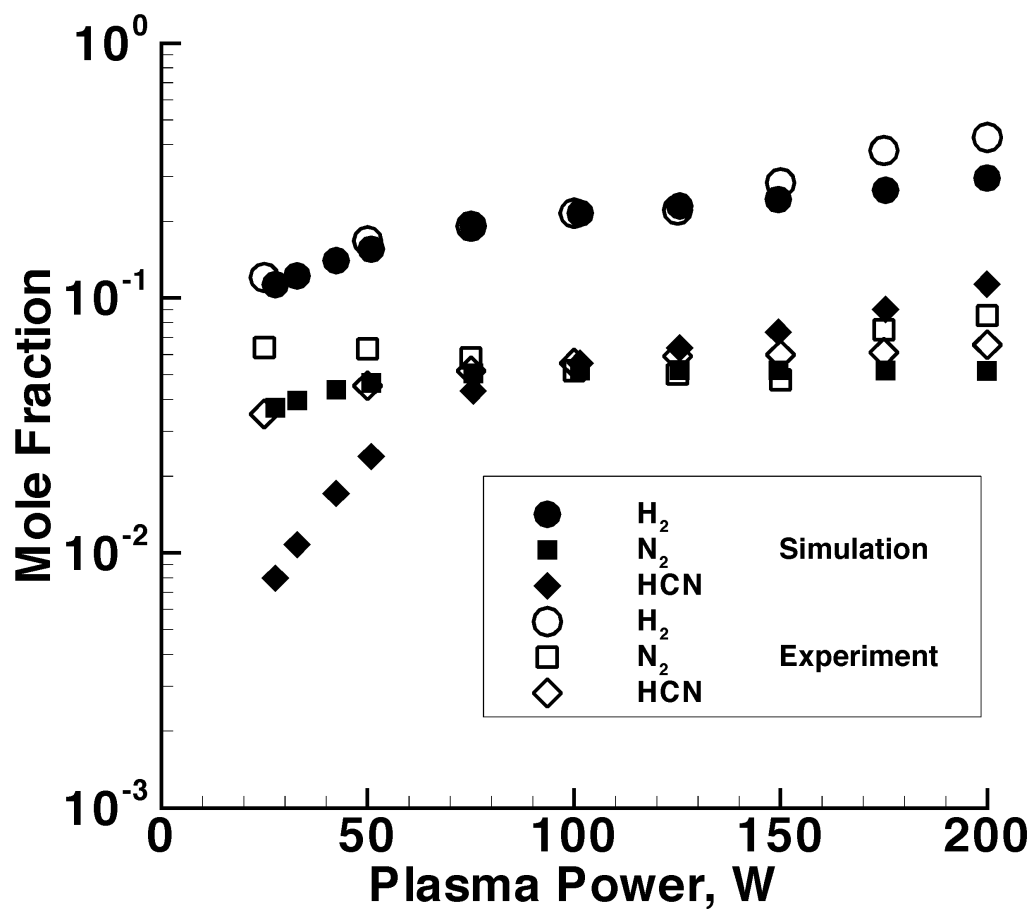


Figure 5. Mole fraction trends of main plasma products from simulation and experiment at one centimeter from cathode.

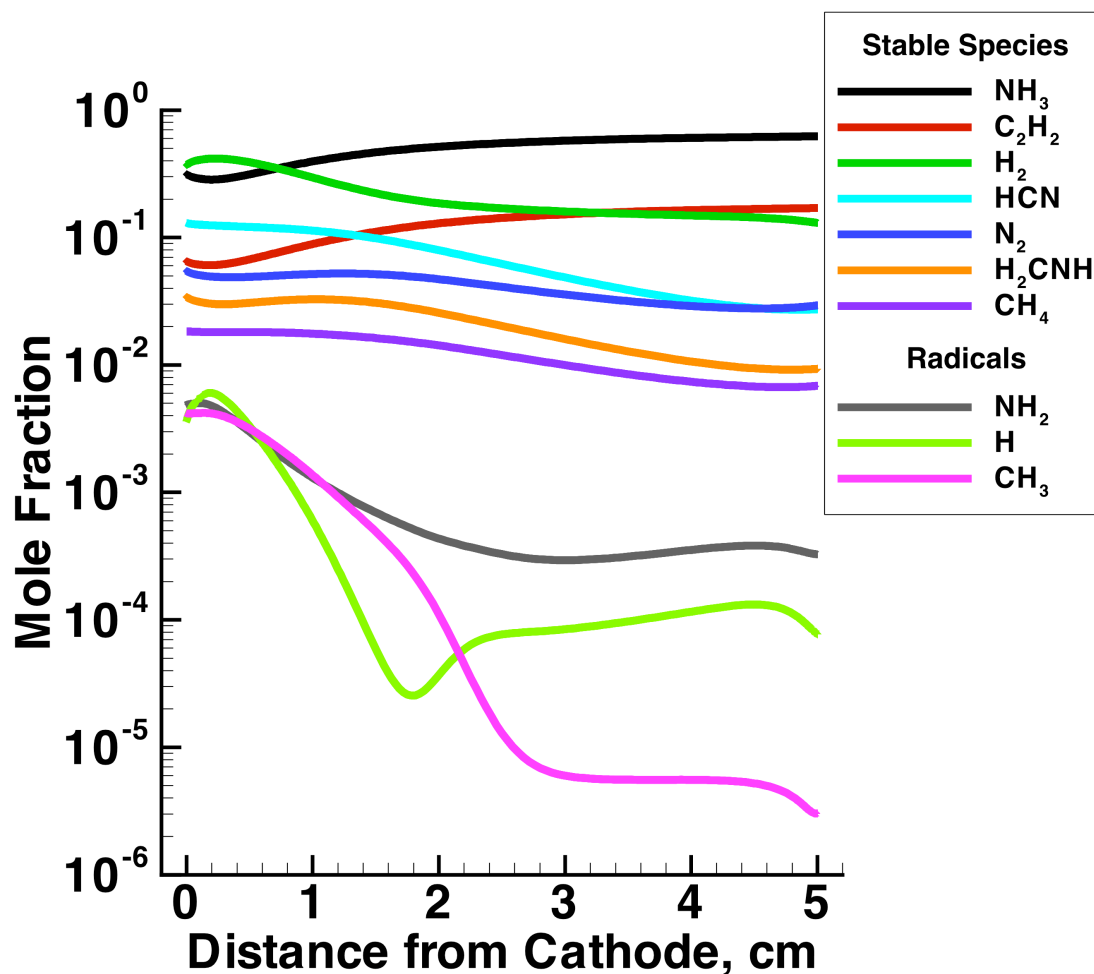


Figure 6. Simulated neutral species in the gas phase at 200 W plasma power plotted versus the distance between the electrodes. The seven most dominant stable species with the three most significant radical species are shown here.

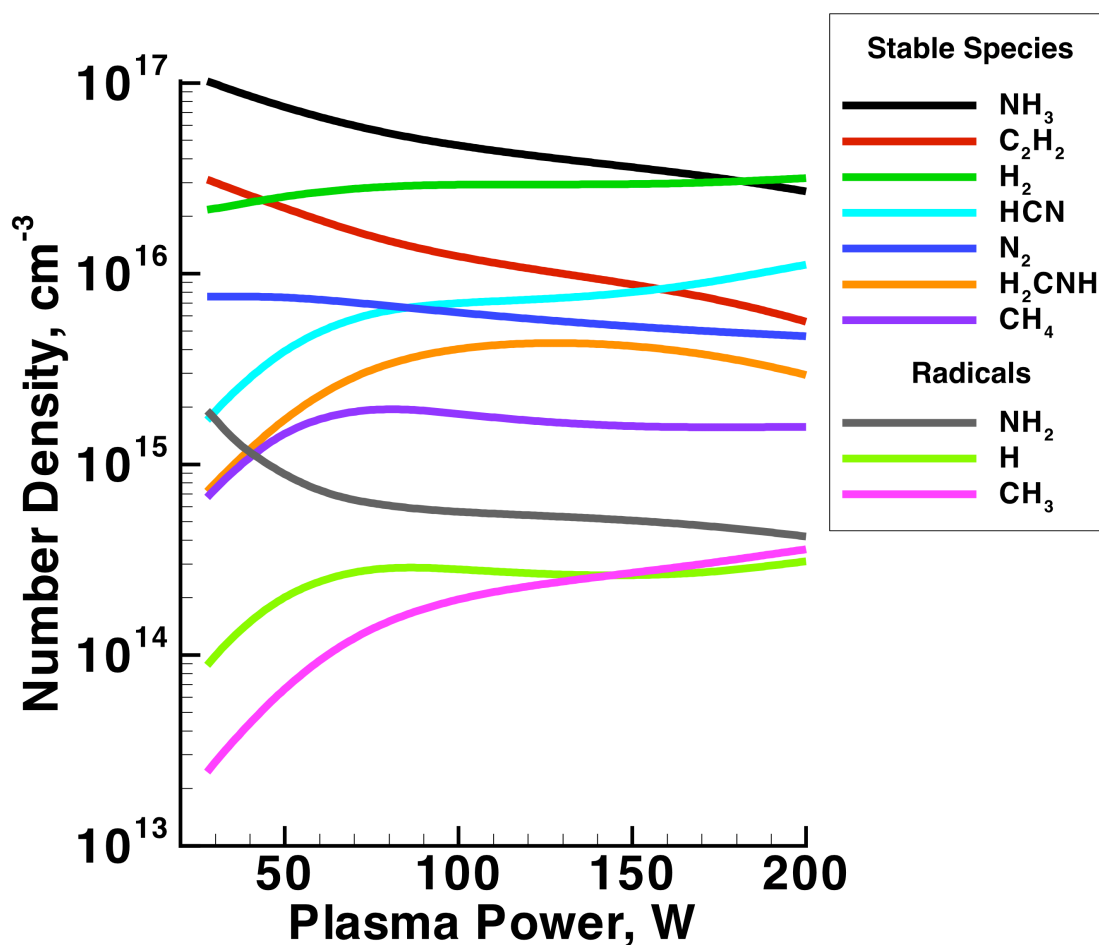


Figure 7. Simulation of the effect of plasma power on gas phase number densities at the substrate where carbon nanotube growth occurs.

-
- (1) Q. Ye, A. M. Cassell, H. Liu, K.-J. Chao, J. Han, and M. Meyyappan, *Nano Lett.* **4**, 1301 (2004).
 - (2) K. K. S. Lau, J. Bico, K. B. K. Teo, M. Chhowalla, G. A. J. Amaratunga, W. I. Milne, G. H. McKinley, and K. K. Gleason, *Nano Lett.* **3**, 1701 (2003).
 - (3) G. Pirio, P. Legagneux, D. Pribat, K. B. K. Teo, M. Chhowalla, G. A. J. Amaratunga, and W. I. Milne, *Nanotechnol.* **13**, 1 (2002).
 - (4) L. Gangloff, E. Minoux, K. B. K. Teo P. Vincent, V. T. Semet, V. T. Binh, M. H. Yang, I. Y. Y. Bu, R. G. Lacerda, G. Pirio, J. P. Schnell, D. Pribat, D. G. Hasko, G. A. J. Amaratunga, W. I. Milne, and P. Legagneux, *Nano Lett.* **4**, 1575 (2004).
 - (5) J. Li, Q. Ye, A. Cassell, H. T. Ng, R. Stevens, J. Han, and M. Meyyappan, *Appl. Phys. Lett.* **82**, 2491 (2003).
 - (6) Q. Ngo, D. Petranovic, S. Krishnan, A. M. Cassell, Q. Ye, J. Li, M. Meyyappan, and C. Y. Yang, *IEEE Trans. Nanotechnol.* **3**, 311 (2004).
 - (7) M. A. Guillorn, A. V. Melechko, V. I. Merkulov, E. D. Ellis, M. L. Simpson, D. H. Lowndes, L. R. Baylor, and G. J. Bordonaro, *J. Vac. Sci. Technol. B* **19**, 2598 (2001).
 - (8) L. R. Baylor, D. H. Lowndes, M. L. Simpson, C. E. Thomas, M. A. Guillorn, V. I. Merkulov, J. H. Wheaton, E. D. Ellis, D. K. Hensley, and A. V. Melechko, *J. Vac. Sci. Technol. B* **20**, 2646 (2002).
 - (9) K. B. K. Teo, M. Chhowalla, G. A. J. Amaratunga, W. I. Milne, P. Legagneux, G. Pirio, L. Gangloff, D. Pribat, V. Semet, V. T. Binh, W. H. Bruenger, J. Eichholz, H. Hanssen, D. Friedrich, S. B. Lee, D. G. Hasko, and H. Ahmed, *J. Vac. Sci. Technol. B* **21**, 693 (2003).

- (10) L. R. Baylor, W. L. Gardner, X. Yang, R. J. Kasica, M. A. Guillorn, B. Blalock, H. Cui, D. K. Hensley, S. Islam, D. H. Lowndes, A. V. Melechko, V. I. Merkulov, D. C. Joy, P. D. Rack, M. L. Simpson, and D. K. Thomas, *J. Vac. Sci. Technol. B* **22**, 3021 (2004).
- (11) L. Zhang, A. V. Melechko, V. I. Merkulov, M. A. Guillorn, M. L. Simpson, D. H. Lowndes, and M. J. Doktycz, *Appl. Phys. Lett.* **81**, 135 (2002).
- (12) B. L. Fletcher, E. D. Hullander, A. V. Melechko, T. E. McKnight, K. L. Klein, D. K. Hensley, J. L. Morrell, M. L. Simpson, and M. J. Doktycz, *Nano Lett.* **4**, 1809 (2004).
- (13) T. E. McKnight, A. V. Melechko, G. D. Griffin, M. A. Guillorn, V. I. Merkulov, F. Serna, D. K. Hensley, M. J. Doktycz, D. H. Lowndes, and M. L. Simpson, *Nanotechnol.* **14**, 551 (2003).
- (14) T. E. McKnight, A. V. Melechko, D. K. Hensley, D. G. J. Mann, G. D. Griffin, and M. L. Simpson, *Nano Lett.* **4**, 1213 (2004).
- (15) M. A. Guillorn, T. E. McKnight, A. Melechko, V. I. Merkulov, P. F. Britt, D. W. Austin, D. H. Lowndes, and M. L. Simpson, *J. Appl. Phys.* **91**, 3824 (2002).
- (16) J. Li, H. T. Ng, A. Cassell, W. Fan, H. Chen, Q. Ye, J. Koehne, J. Han, and M. Meyyappan, *Nano Lett.* **3**, 597 (2003).
- (17) J. Koehne, H. Chen, J. Li, A. M. Cassell, Q. Ye, H. T. Ng, J. Han, and M. Meyyappan, *Nanotechnol.* **14**, 1239 (2003).
- (18) Y. Lin, F. Lu, Y. Tu, and Z. Ren, *Nano Lett.* **4**, 191 (2004).
- (19) T. E. McKnight, A. V. Melechko, D. W. Austin, T. Sims, M. A. Guillorn, and M. L. Simpson, *J. Phys. Chem. B* **108**, 7115 (2004).
- (20) Y. Avigal and R. Kalish, *Appl. Phys. Lett.* **78**, 2291 (2001).

- (21) Y. Zhang, A. Chang, J. Cao, Q. Wang, W. Kim, Y. Li, N. Morris, E. Yenilmez, J. Kong, and H. Dai, *Appl. Phys. Lett.* **79**, 3155 (2001).
- (22) A. Ural, Y. Li, and H. Dai, *Appl. Phys. Lett.* **81**, 3464 (2002).
- (23) L. Delzeit, R. Stevens, C. Nguyen, and M. Meyyappan, *Int. J. Nanoscience* **1**, 197 (2002).
- (24) E. Joselevich and C. M. Lieber, *Nano Lett.* **2**, 1137 (2002).
- (25) Z. F. Ren, Z. P. Huang, J. W. Xu, J. H. Wang, P. Bush, M. P. Siegal, and P. N. Provencio, *Science* **282**, 1105 (1998).
- (26) K. B. K. Teo, M. Chhowalla, G. A. J. Amaratunga, W. I. Milne, D. G. Hasko, G. Pirio, P. Legagneux, F. Wyczisk, and D. Pribat, *Appl. Phys. Lett.* **79**, 1534 (2001).
- (27) M. Chhowalla, K. B. K. Teo, C. Ducati, N. L. Rupesinghe, G. A. J. Amaratunga, A. C. Ferrari, D. Roy, J. Robertson, and W. I. Milne, *J. Appl. Phys.* **90**, 5308 (2001).
- (28) V. I. Merkulov, A. V. Melechko, M. A. Guillorn, M. L. Simpson, D. H. Lowndes, J. H. Whealton, and R. J. Raridon, *Appl. Phys. Lett.* **80**, 4816 (2002).
- (29) Q. Yang, C. Xiao, W. Chen, A. K. Singh, T. Asai, and A. Hirose, *Diamond Relat. Mater.* **12**, 1482 (2003).
- (30) Ch. Täschner, F. Pácal, A. Leonhardt, P. Spatenka, K. Bartsch, A. Graff, and R. Kaltofen, *Surf. Coat. Technol.* **174-175**, 81 (2003).
- (31) J. F. AuBuchon, L.-H. Chen, A. I. Gapin, D.-W. Kim, C. Daraio, and S. Jin, *Nano Lett.* **4**, 1781 (2004).
- (32) T. Ikuno, H. Furuta, T. Yamamoto, S. Takahashi, M. Kamizono, S. Honda, M. Katayama, T. Hirao, and K. Oura, *Surf. Interface Anal.* **35**, 15 (2003).
- (33) T. Kato, G.-H. Jeong, T. Hirata, R. Hatakeyama, K. Tohji, and K. Motomiya, *Chem. Phys. Lett.* **381**, 422 (2003).

- (34) T. Kato, G.-H. Jeong, T. Hirata, and R. Hatakeyama, *Thin Solid Films* **457**, 2 (2004).
- (35) Y. Li, D. Mann, M. Rolandi, W. Kim, A. Ural, S. Hung, A. Javey, J. Cao, D. Wang, E. Yenilmez, Q. Wang, J. Gibbons, Y. Nishi, and H. Dai, *Nano Lett.* **4**, 317 (2004).
- (36) S. H. Tsai, C. W. Chao, C. L. Lee, and H. C. Shih, *Appl. Phys. Lett.* **74**, 3462 (1999).
- (37) C. Bower, W. Zhu, S. Jin, and O. Zhou, *Appl. Phys. Lett.* **77**, 830 (2000).
- (38) M. Chen, C.-M. Chen, and C.-F. Chen, *Thin Solid Films* **420-421**, 230 (2002).
- (39) L. Delzeit, I. McAninch, B. A. Cruden, D. Hash, B. Chen, J. Han, and M. Meyyappan, *J. Appl. Phys.* **91**, 6027 (2002).
- (40) L. Delzeit, C. V. Nguyen, R. M. Stevens, J. Han, and M. Meyyappan, *Nanotechnol.* **13**, 280 (2002).
- (41) K. Matthews, B. A. Cruden, B. Chen, M. Meyyappan, and L. Delzeit, *J. Nanosci. Nanotechnol.* **2**, 475 (2002).
- (42) J. B. O. Caughman, L. R. Baylor, M. A. Guillorn, V. I. Merkulov, D. H. Lowndes, and L. F. Allard, *Appl. Phys. Lett.* **83**, 1207 (2003).
- (43) S. Honda, M. Katayama, K. Lee, T. Ikuno, S. Ohkura, K. Oura, H. Furuta, and T. Hirao, *Jpn. J. Appl. Phys.* **42**, L441 (2003).
- (44) K. Lee, M. Katayama, S. Honda, T. Kuzuoka, T. Miyake, Y. Terao, J. Lee, H. Mori, T. Hirao, and K. Oura, *Jpn. J. Appl. Phys.* **42**, L804 (2003).
- (45) C. M. Hsu, C. H. Lin, H. L. Chang, and C. T. Kuo, *Thin Solid Films* **420-421**, 225 (2002).
- (46) Y. S. Woo, D. Y. Jeon, I. T. Han, Y. J. Park, H. J. Kim, J. E. Jung, J. M. Kim, and N. S. Lee, *J. Vac. Sci. Technol. B* **21**, 1660 (2003).

- (47) C. H. Lin, S. H. Lee, C. M. Hsu, and C. T. Kuo, *Diamond Relat. Mater.* **13**, 2147 (2004).
- (48) C. C. Lin, I. C. Leu, J. H. Yen, and M. H. Hon, *Nanotechnol.* **15**, 176 (2004).
- (49) Y. S. Woo, D. S. Jeon, I. T. Han, N. S. Lee, J. E. Jung, and J. M. Kim, *Diamond Relat. Mater.* **11**, 59 (2002).
- (50) B. A. Cruden, A. M. Cassell, Q. Ye, and M. Meyyappan, *J. Appl. Phys.* **94**, 4070 (2003).
- (51) I. B. Denysenko, S. Xu, J. D. Long, P. P. Rutkevych, N. A. Azarenkov, and K. Ostrikov, *J. Appl. Phys.* **95**, 2713 (2004).
- (52) M. S. Bell, R. G. Lacerda, K. B. K. Teo, N. L. Rupesinghe, G. A. J. Amaratunga, W. I. Milne, and M. Chhowalla, *Appl. Phys. Lett.* **85**, 1137 (2004).
- (53) B. A. Cruden, A. M. Cassell, D. B. Hash, and M. Meyyappan, *J. Appl. Phys.* **96**, 5284 (2004).
- (54) D. Hash, D. Bose, T. R. Govindan, and M. Meyyappan, *J. Appl. Phys.* **93**, 6284 (2003).
- (55) B. L. Peko, R. L. Champion, M. V. V. S. Rao, and J. K. Olthoff, *J. Appl. Phys.* **92**, 1657 (2002).
- (56) B. L. Peko, I. V. Dyakov, and R. L. Champion, *J. Chem. Phys.* **109**, 5269 (1998).
- (57) J. F. O'Hanlon, *A User's Guide to Vacuum Technology* (Wiley, New York, 1980), p. 105-119.
- (58) *NIST Chemistry WebBook*, <http://webbook.nist.gov>
- (59) A. J. Dean, R. K. Hanson, and C. T. Bowman, *J. Phys. Chem.* **95**, 3180 (1991).

- (60) K. B. K. Teo, D. B. Hash, R. G. Lacerda, N. L. Rupesinghe, M. S. Bell, S. H. Dalal, D. Bose, T. R. Govindan, B. A. Cruden, M. Chhowalla, G. A. J. Amaratunga, M. Meyyappan, and W. I. Milne, *Nano Lett.* **4**, 921 (2004).
- (61) D. R. Lide (Ed.), *CRC Handbook of Chemistry and Physics*, 81st Edition (CRC Press, Boca Raton, 2000).
- (62) V. G. Anicich, *J. Phys. Chem. Ref. Data* **22**, 1469 (1993).
- (63) L. Operti, R. Rabazzana, and G. A. Vaglio, *Int. J. Mass Spectrom.* **228**, 403 (2003).
- (64) L. Operti, R. Rabazzana, F. Turco, and G. A. Vaglio, *Int. J. Mass Spectrom.* **232**, 139 (2004).
- (65) V. G. Anicich and M. J. McEwan, *Planet. Space Sci.* **45**, 897 (1997).
- (66) C. N. Keller, T. E. Cravens, and L. Gan, *J. Geophys. Res.* **97**, 12117 (1992).
- (67) A. V. Phelps, *J. Phys. Chem. Ref. Data* **19**, 653 (1990).